ACCEPTED ARTICLE PREVIEW

Accepted Article Preview: Published ahead of online publication

Table-top extreme ultraviolet Grazing-Reflection Ptychography with Full-Pose Self-Calibration

Yanqi Chen, Hao Xu, Qingxin Wang, Yanwei Li, Lei Huang, Zhengkang Xu, Su Li, Dongliang Wang, Yaqi Wu, Jianjie Li, Fei Wang, Xiaoshi Zhang, Bowen Liu, Guoqing Chang, Jie Li, Changjun Ke, Yishi Shi, Zhongwei Fan

Cite this article as: Yanqi Chen, Hao Xu, Qingxin Wang, Yanwei Li, Lei Huang, Zhengkang Xu, Su Li, Dongliang Wang, Yaqi Wu, Jianjie Li, Fei Wang, Xiaoshi Zhang, Bowen Liu, Guoqing Chang, Jie Li, Changjun Ke, Yishi Shi, Zhongwei Fan. Table-top extreme ultraviolet Grazing-Reflection Ptychography with Full-Pose Self-Calibration. *Light: Advanced Manufacturing* accepted article preview 30 June, 2026; doi: 10.37188/lam.2026.112

This is a PDF file of an unedited peer-reviewed manuscript that has been accepted for publication. LAM are providing this early version of the manuscript as a service to our customers. The manuscript will undergo copyediting, typesetting and a proof review before it is published in its final form. Please note that during the production process errors may be discovered which could affect the content, and all legal disclaimers apply.

Received 2 June 2026; revised 30 June 2026; accepted 30 June 2026;
Accepted article preview online 30 June 2026

Accepted Manuscript

ACCEPTED ARTICLE PREVIEW

Table-top extreme ultraviolet Grazing-Reflection Ptychography with Full-Pose Self-Calibration

Yanqi Chen[1,2†], Hao Xu[3†], Qingxin Wang[1,2†], Yanwei Li[9†], Lei Huang[1,2,3], Zhengkang Xu[1,3], Su Li[1,2], Dongliang Wang[4,5], Yaqi Wu[7,8], Jianjie Li[9], Fei Wang[10], Xiaoshi Zhang[11,12], Bowen Liu[7,8], Guoqing Chang[4,5,6], Jie Li[1,3], Changjun Ke[3], Yishi Shi[1,2,3,*], Zhongwei Fan[1,3]

[1] School of Optoelectronics, University of Chinese Academy of Sciences, Beijing, 100190, Beijing, China.

[2]Center for Materials Science and Optoelectronics Engineering, Chinese Academy of Sciences,Beijing, 100190, Beijing, China.

[3]Aerospace Information Research Institute, Chinese Academy of Sciences,Beijing, 100190, Beijing, China.

[4]Beijing National Laboratory for Condensed Matter Physics, Institute of Physics, Chinese Academy of Sciences, Beijing, 100190, Beijing, China.

[5] School of Physics, Chinese Academy of Sciences, Beijing, 100190, Beijing, China.

[6] Songshan Lake Materials Laboratory, Dongguan, 523808, Guangdong Province, China.

[7] Ultrafast Laser Laboratory, Key Laboratory of Opto-Electronic Information Science and Technology of Ministry of Education, School of Precision Instruments and Opto-Electronics Engineering, Tianjin University, Tianjin, 300072, Tianjin, China.

[8] Georgia Tech Shenzhen Institute, Tianjin University, Shenzhen, 518071, Guangdong Province, China.

[9] Jihua Laboratory, Foshan, 518071, Guangdong Province, China.

[10]Wangzhijiang Innovation Center for Laser, Aerospace Laser Technology and System Department, Shanghai Institute of Optics and Fine Mechanics, Chinese Academy of Sciences,Shanghai, 201800, Shanghai, China.

[11]Southwest United Graduate School, Yunnan University, Kunming, 650500, Yunnan, China.

Accepted Manuscript

ACCEPTED ARTICLE PREVIEW

047
048
049
050
051
052
053
054
055
056
057
058
059
060
061
062
063
064
065
066
067
068
069
070
071
072
073
074
075
076
077
078
079
080
081
082
083
084
085
086
087
088
089
090
091
092

[12]School of Physics and Astronomy, Yunnan University, Kunming, 650500, Yunnan, China.
*Corresponding Author.

†These authors contributed equally to this work.

Abstract

Table-top extreme ultraviolet (EUV) reflection ptychography has gained increasing interest in semiconductor metrology due to its nanometer-scale resolution, nondestructive character, and laboratory-scale cost-effectiveness. However, its widespread adoption remains constrained by alignment challenges inherent to grazing-reflection geometry, which have prevented reflective configurations from achieving image quality comparable to those of transmission-mode systems. In this study, we introduce a table-top EUV grazing-reflection ptychography system that enables full-pose self-calibration through holistic system modeling and highly efficient optimization. The developed system is validated using a customized wafer sample and real chip sample. Experimental results indicate that the system successfully corrects image distortions, improves resolution, and enhances surface metrology quality. Furthermore, we discuss algorithmic and physical issues including the feature-domain phase-retrieval for ptychography and coupling effect among pose parameters. The proposed approach not only accelerates the transition of EUV reflection ptychography toward real-world use but also opens avenues for methodological advances to a wider range of imaging applications.

Keywords: Extreme ultraviolet, reflection imaging, ptychography, self-calibration

Accepted Manuscript

ACCEPTED ARTICLE PREVIEW

1 Introduction

As semiconductor manufacturing progresses toward nanometer-scale features, there is an escalating demand for advanced metrology that can address critical dimensions and overlay errors [1]. Short-wavelength techniques such as extreme ultraviolet (EUV) imaging offer distinct advantages [2, 3], including nanometer resolution, deep penetration, and nondestructive inspection, making them suitable for semiconductor metrology. Furthermore, the development of tabletop EUV sources based on high harmonic generation provides high brightness and coherence, effectively facilitating laboratory-scale imaging [4–6].

However, progress in EUV-based metrology has been hindered in recent years by several fundamental challenges. A primary obstacle is the scarcity of high-quality, high numerical aperture (NA) optics suitable for this spectral band. Within the EUV regime (approximately 10–100 nm), all materials strongly absorb radiation, necessitating the use of mirrors instead of lenses. The fabrication of these EUV mirrors demands specially designed multilayer coatings and exceptional surface smoothness, with height variations significantly smaller than the wavelength. These rigid requirements render EUV mirrors extremely difficult and costly to manufacture [7–9].

Ptychography has opened new avenues for lensless imaging [10–12]. Unlike conventional approaches that rely on complex optical systems, ptychography does not require any optical elements between the sample and detector; instead, it reconstructs the sample image directly from diffraction patterns. By leveraging redundant information from spatially overlapped scanning, ptychography recovers the illumination probe and image nonisolated specimens [13–16]. The NA in this technique is determined by the diffraction distance and detector size, and therefore, it approaches the theoretical limit [17]. Thus far, ptychography in transmission geometry has proven to be an effective tool for high-resolution imaging in the EUV waveband, and several studies demonstrated its utilization in the analysis of lithographic components [11, 18, 19] and biological samples [20, 21], and in the multiwavelength characterization of EUV optics [22, 23]. However, the application of EUV ptychography in reflection configurations remains limited.

In practice, EUV reflection ptychography can be implemented across three distinct ranges of reflection angles: small angles ($<10°$) [24–26], which are commonly used for photomask inspection in lithography; moderate angles ($<60°$) [27, 28], typically employed to explore the fundamental principles of reflective diffraction imaging and seldom applied in practical inspection tasks; and large reflection angles ($\sim 70°$) [29–32], which corresponds to grazing-reflection geometry. Within this grazing reflection range, most materials are reflective, and the phase response shows significant angular sensitivity, making it suitable for tasks such as defect analysis and compositional analysis in semiconductor inspection. Further, reflective diffraction imaging at other wavelengths uses grazing reflection systems [31, 33].

However, such a grazing-reflection configuration poses significant challenges to system alignment and calibration for ptychography. Moreover, the limited power of tabletop EUV sources results in weak reflected and diffracted signals. Consequently, the effect of system misalignment is exacerbated by a low signal-to-noise ratio (SNR), which significantly degrades imaging quality. This issue becomes pronounced for larger

Accepted Manuscript

ACCEPTED ARTICLE PREVIEW

139 numerical apertures, wherein the high-frequency signal content is sparse. Transmission
140 ptychography involves calibrating the diffraction distance and scan positions, which is
141 a subject thoroughly addressed in many studies [34–37]. However, calibration methods
142 for reflection ptychography remain relatively underdeveloped.

143 Although some efforts have been made to correct system misalignment [38–40],
144 they are constrained by the oversimplified assumption that all parameters are correct,
145 except for one or two corrections. Maintaining this assumption requires using highly
146 precise hardware alignment solutions, which undoubtedly increase system cost and
147 complexity and hinder its general applicability in practical scenarios. Further, this
148 assumption remains unrealistic even with highly sophisticated hardware alignments
149 because of inevitable discrepancies between idealized models and real physical systems.
150 Consequently, improvements in image quality remain limited. Thus far, there is no
151 comprehensive and holistic solution that can perform the integrated calibration of full-
152 pose parameters in reflection ptychography systems, and the need for such a solution
153 is genuine and urgent.

154 In this study, we report a grazing-reflection ptychography system operating on a
155 17.9 nm table-top EUV source that features full-pose self-calibration capability. The
156 full-pose calibration is based on an advanced optimization framework that includes
157 comprehensive system modeling, feature domain phase retrieval, and automatic dif-
158 ferentiation. The system is used to image a customized sample and a real chip, and
159 the proposed self-calibration algorithm demonstrates an unprecedented improvement
160 in image quality. Our method addresses a fundamental challenge in reflection pty-
161 chography and significantly advances its practical application. This study has inspired
162 progress in diffraction-based imaging techniques across broader regimes, including
163 visible light, X-ray, and electron microscopy.
164

165 # 2 Results
166

167 ## 2.1 Principle
168

169 In transmission ptychography, the camera is placed parallel to the sample to capture
170 diffraction signals in reciprocal space after the illumination probe interacts with the
171 specimen. These signals are distributed in the Ewald sphere. Under paraxial approx-
172 imation with a low numerical aperture, the pixel array on the detection plane can
173 sample the reciprocal space diffraction signal uniformly. In the EUV reflection pty-
174 chography system (Fig. 1a), the detector is positioned perpendicular to the outgoing
175 light but tilted relative to the sample. This configuration leads to the nonuniform sam-
176 pling of the reciprocal space signal on the Ewald sphere. Diffraction patterns appear
177 significantly distorted compared to those under normal-incidence illumination. In con-
178 ventional approaches, the degraded imaging performance in reflection ptychography
179 is largely attributed to the insufficient correction of this distortion.

180 To address this issue, we describe the mapping relationship $\mathbf{T}$ between the diffrac-
181 tion pattern distributed on the Ewald sphere and tilted detector plane as a function
182 of the pose parameters of the reflection system, including diffraction distance d, three-
183 dimensional illumination angle $\boldsymbol{\theta} = [\theta_x, \theta_y, \theta_z]^\top$, and three-dimensional detection
184 rotation angle $\boldsymbol{\gamma} = [\gamma_x, \gamma_y, \gamma_z]^\top$. A detailed derivation of the mapping operator $\mathbf{T}$ is

Accepted Manuscript

ACCEPTED ARTICLE PREVIEW

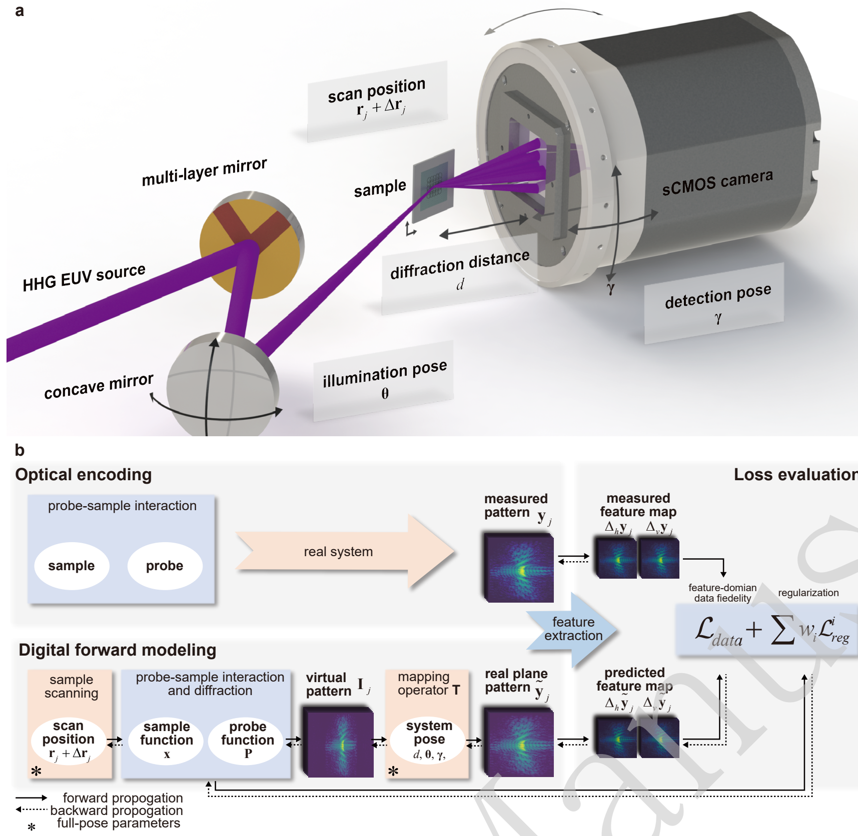

Fig. 1 Principle of full-pose self-calibration for table-top EUV reflection ptychography. **a** Schematic of table-top EUV reflection ptychography system with grazing illumination. Misalignment attributed to scan position, diffraction distance, illumination pose, and detection pose. **b** Flow work of proposed method. The optical encoding block represents a physical experimental setup, whereas the digital forward modeling block simulates how system parameters are combined to generate predicted diffraction patterns. Following loss evaluation using a feature-domain (FD) loss function along with regularization terms, the gradients of each variable are computed via auto-differentiation and back-propagated. Finally, variables are updated using an optimizer.

provided in the Materials and Methods section. As depicted by the digital forward modeling block in Fig.1b, we further integrate this relationship into the forward model of ptychography.

$$\mathbf{y}_j = \mathbf{T}\left\{\mathbf{I}_j = \left|\mathbf{A}\left[\mathbf{P}\odot\mathbf{Q}_j\left(\mathbf{x},\mathbf{r}_j+\Delta\mathbf{r}_j\right)\right]\right|^2, d, \boldsymbol{\theta}, \boldsymbol{\gamma}\right\}, j = 1, 2, ..., N \tag{1}$$

where $\mathbf{y}_j$, $\mathbf{I}_j$, $\mathbf{A}$, $\mathbf{P}$, $\mathbf{x}$, $\mathbf{Q}_j$, $\mathbf{r}_j$, and $\Delta\mathbf{r}_j = [\Delta x_j, \Delta y_j]^\top$ represent the jth diffraction pattern in total N frames, virtual pattern on the Ewald sphere, propagation operator, probe function, sample function, translation operator, two-dimensional estimated scan position, and position error, respectively. The scan position error is integrated

Accepted Manuscript

ACCEPTED ARTICLE PREVIEW

231 using the Fourier shift theorem [?]. After modeling the full-pose integrated forward
232 propagation, we use the feature domain (FD) loss [42, 43] for data fidelity assessment
233 between the measurement $\mathbf{y}_j$ and prediction $\tilde{\mathbf{y}}$.
234
235
236
237
238

$$\mathcal{L}_{data} = \sum_{j=1}^{N} \left\| \nabla \sqrt{\mathbf{y}_j} - \nabla \sqrt{\tilde{\mathbf{y}}_j} \right\|_{Huber} \tag{2}$$

239 where $\nabla = [\nabla_x, \nabla_y]^\top$ represents the first-order differentiation operator. Further,
240 $\|\cdot\|_{Huber}$ represents the Huber norm [44], which is a hybrid loss function combining L_1
241 and L_2 components to balance robustness against outliers with optimization efficiency.
242 Compared to the element-wise loss functions such as the mean squared error (MSE)
243 used in traditional phase retrieval, the FD loss is less sensitive to model degeneration.
244 Prior knowledge can be incorporated through regularization terms to enhance
245 reconstruction stability, including support and denoising constraints. The complete
246 loss function is expressed as $\mathcal{L}_{full} = \mathcal{L}_{data} + \sum_i w_i \mathcal{L}^i_{reg}$, where w_i represents the
247 weighting coefficient of the ith regularization term. The complete workflow of the pro-
248 posed method is shown in Fig. 1b. The optical encoding block represents the physical
249 measurement process in the actual system, whereas the digital forward modeling block
250 implements computational mapping from variables to the predictions. The loss func-
251 tion evaluates and backpropagates through a computational graph for accumulating
252 the gradients of each variable using automatic differentiation. Materials and Meth-
253 ods present more details about the implementation of the experimental algorithm,
254 including the sampling conditions, regularization, and optimizer settings.
255 We conducted a series of investigations into method performance and system
256 behavior after completing the forward modeling and inverse problem design. The
257 following investigations provide profound algorithmic and physical insights into reflec-
258 tion ptychography, which offers essential guidance for robust algorithm designs and
259 optimized experimental configurations:
260 **I**. We validate the effectiveness of the FD loss function used in ptychography.
261 Simulations are performed under different illumination doses and source coherence
262 conditions. The detailed implementation is provided in Section S1. As shown in Figs.
263 S1 and S2, the FD-Huber loss successfully recovered images under moderate noise
264 levels and coherence degradation, outperforming both MSE and FD-L_1 loss. This
265 conclusion is corroborated by experimental results shown in Fig. S3.
266 **II**. In Section S2, we explore the sensitivity of image reconstruction to different pose
267 parameters under varying reflection angle settings with simulation results presented
268 in Fig. S4. We find that misalignment in all parameters can degrade reconstruction
269 quality. The sensitivity to misalignments in θ_x, θ_y, and $\Delta\mathbf{r_j}$ increases significantly
270 as the geometry approaches grazing reflection. This sensitivity analysis explains why
271 grazing-reflection ptychography yields poorer image reconstruction quality compared
272 to normal-incidence or small-angle illumination and underscores the necessity of full-
273 pose self-calibration.
274 **III**. We identify coupling relationships among the parameters, which are dis-
275 cussed in detail in Section S3. Parameter coupling indicates that the error of one
276 parameter can be compensated by adjusting other parameters. This effect is most

Accepted Manuscript

ACCEPTED ARTICLE PREVIEW

pronounced between the pose parameters and scan positions. Consequently, we introduce a segmented updating optimization strategy to decouple parameters during self-calibration.

IV. We discuss the illumination-dose dependence of full-pose self-calibration. The simulation results in Section S4 indicate that full-pose self-calibration is effective when the illumination dose reaches or exceeds 10^7 photons.

277 278 279 280 281 282 283 284 285 286 287 288 289 290 291 292 293 294 295 296 297 298 299 300 301 302 303 304 305 306 307 308 309 310 311 312 313 314 315 316 317 318 319 320 321 322

Accepted Manuscript

ACCEPTED ARTICLE PREVIEW

2.2 Self-calibrated reflection ptychography on 17.9 nm EUV beamline

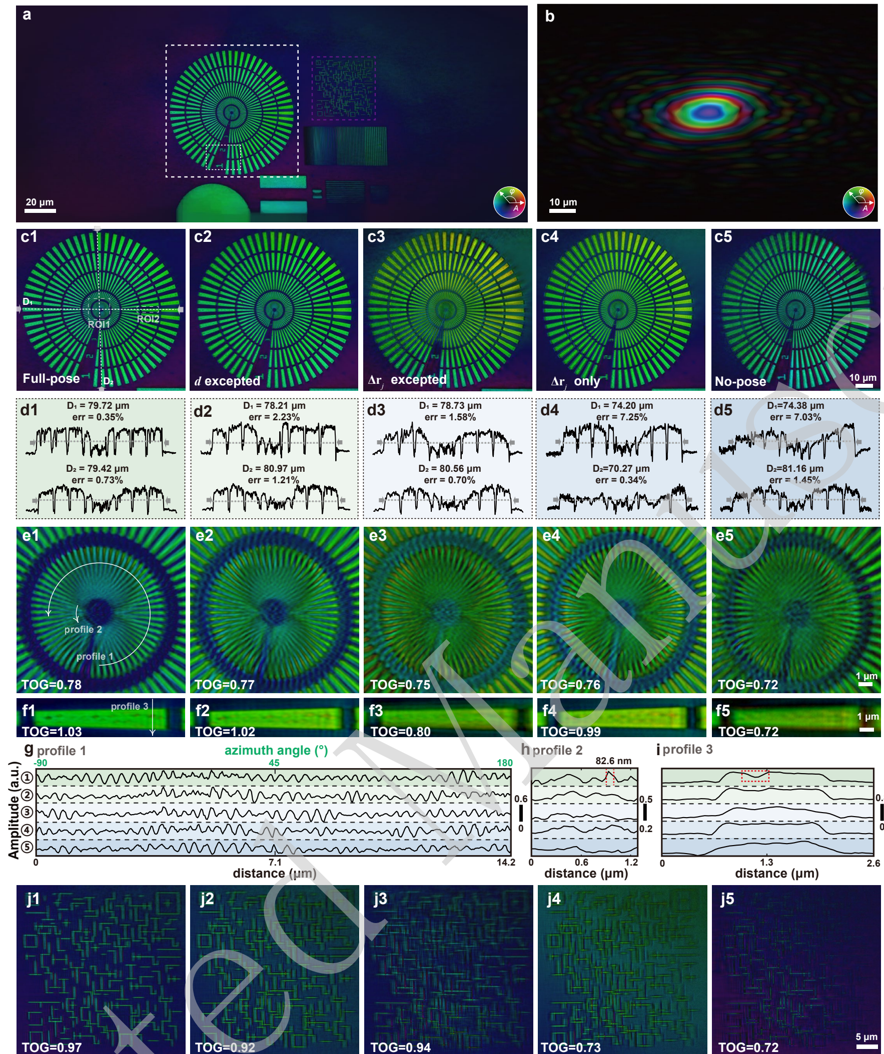

Fig. 2 Imaging results of the customized wafer sample. **a** Full-field pseudocolor image of the reconstructed sample. **b** Pseudocolor image of the reconstructed probe. Amplitude (A) and phase information (φ) correspond to the brightness and hue in the pseudo-color image, respectively. **c1–c5** are magnified Siemens star patterns reconstructed with different calibration strategies; **d1–d5** are amplitude profiles and the measured diameter along D_1 and D_2; **e1–e5** and f1–f5 show magnified images of ROI1 and ROI2 in **c1–c5**; and amplitude profiles 1–3 are plotted in **g–i**. **j1–j5** show magnified maze patterns (marked by purple dashed box in **a**) reconstructed with different strategies.

Accepted Manuscript

ACCEPTED ARTICLE PREVIEW

Table 1 Calibrated pose parameter values on the customized wafer sample with different strategies.

	d (mm)	$\boldsymbol{\theta}$ (°)	$\boldsymbol{\gamma}$ (°)
No pose/$\Delta\mathbf{r}_j$ only	50.00	[0.00, 70.00, 0.00]	[0.00, 0.00, 0.00]
Full pose	48.42	[-0.80, 71.72, 0.35]	[9.13, 2.23, 0.01]
Partial pose: d excepted	50.00	[-0.42, 70.94, 0.15]	[4.13, 2.18, 0.01]
Partial pose: $\Delta\mathbf{r}_j$ excepted	49.44	[-8.30, 71.37, 0.18]	[4.42, 0.39, 0.01]

Our reflection ptychography system uses a table-top 17.9 nm EUV source based on high-order harmonic generation (HHG). Detailed information is provided in Section S7. The focused 17.9 nm beam illuminates the sample at a grazing angle, and a scientific complementary metal–oxide–semiconductor (sCMOS) camera (Dhyana XF95, 2048×2048, 11 μm pixel size) was placed perpendicular to the reflected beam. Incidence angles relative to the normal and sample-camera distances of the sample surface were 70° and 50 mm in the design, respectively. Sample scanning was driven by a two-dimensional slip-stick piezo stage (LS35x.Lab, MultiFields Technology).

In this experiment, we employed a Fermat spiral-scanning strategy with 400 positions [45] and scanning overlap ratio of $\sim$ 82%. At each position, four patterns were recorded with increasing exposure times to enable high dynamic range image fusion. Data recording at each position took approximately 1 s, whereas stage movement and stabilization required approximately 1.2 s. Full data acquisition was completed within approximately 15 min.

The pseudocolor imaging results of a customized wafer sample (silicon substrate with a gold pattern; scanning electron microscope (SEM) image provided in Fig. S9) and corresponding probe functions are presented in Figs. 2 (a) and 2b)). The probe inherently carries a linear phase gradient along the horizontal direction because of the highly tilted illumination. However, in our forward model (mapping operator $\mathbf{T}$), this linear phase term is equivalently represented as a translation of the wavevector coordinates of the Ewald sphere. Consequently, the reconstructed probe wavefront does not explicitly contain this phase component. The pixel size of the reconstructed image is 43.5 nm × 70.0 nm at a numerical aperture (NA) of 0.19 × 0.095. Table 1 lists posture parameter values under their default settings ($d = 50$ mm, $\theta_y = 70$, and rest = 0) and after calibration using different strategies. Figs. 2c1–c5 show the overall outline of the Siemens star pattern reconstructed with full-pose, partial-pose, and no-pose calibrations. The outer diameter of the Siemens star pattern is 80 μm, and the pattern includes five groups of radial gratings from the outside with a minimum line width of 30 nm.

The outer diameters are measured in the horizontal (D1) and vertical (D2) directions for images reconstructed using different strategies (Figs. 2d1–d5). The reconstructed patterns exhibit severe compression in the horizontal direction when the scan position error ($\Delta\mathbf{r}_j$) is calibrated without pose parameters or when no calibration is performed. This perspective distortion stems from inaccurate θy estimations, leading to incorrect sampling intervals in the reciprocal space. In contrast, calibrating

Accepted Manuscript

ACCEPTED ARTICLE PREVIEW

415 pose parameters while neglecting $\Delta \mathbf{r}_j$ partially alleviates the distortion. The full-
416 pose strategy yields the smallest errors, with both D1 and D2 deviations below 1%,
417 outperforming other strategies including the one in which d is fixed.
418 Figs. 2e1–e5 display the central region (ROI1) of the Siemens star pattern. Images
419 reconstructed without full-pose parameters show artifacts and reduce contrast near
420 the center (Figs. 2e2–e5). The corresponding amplitude profiles (No. 1 in Figs. 2g)
421 and (h) confirm this observation. Figs. S9b and d in Section S6 provide a direct
422 visual comparison of Siemens star patterns under an SEM and full-pose EUV pattern,
423 which shows high consistency between two modalities. For quantitative comparison,
424 we calculate the Tamura coefficient of the gradient (TOG), which is a metric that
425 characterizes the clarity of the complex-field image within each ROI [46]. TOG values
426 align with the visual assessment, which confirms that full-pose reconstruction yield
427 the sharpest results. However, grating features are not fully resolved even in full-pose
428 reconstruction, and the horizontal gratings appear clearer than the vertical gratings.
429 This discrepancy can be attributed to the anisotropic nature of the NA of the system.
430 Profile No. 1 in Fig. 2 h indicates that the full width at half-maximum (FWHM) of
431 the measured minimum grating is 82.6 nm, which is approximately equal to 1.9 pixel
432 sizes. Images of ROI2, which contain a larger line pattern with punctate defects, are
433 shown in Figs. 2f1–f5. As demonstrated by the profiles in Fig. 2 (i), only the full-pose
434 strategy successfully resolved the defects.
435 Figs. 2j1–j5 show enlarged views of the maze pattern, and a direct comparison with
436 the SEM image is shown in Figs. S9 c and e. With full-pose self-calibration, the EUV
437 image clearly resolved both the horizontal and vertical lines while presenting a flat
438 background, thereby indicating high consistency with the SEM image. In contrast, all
439 other strategies were severely contaminated by artifacts.
440 In EUV reflection ptychography, material-specific surface characterization is
441 enabled by rich information in the complex-field imaging mode. The amplitude of the
442 complex value corresponds to the reflectance at each pixel, whereas its phase angle
443 reflects the phase change induced by the interface phase shift governed by Fresnel
444 relations and surface topography of the sample. The quality of sample characteriza-
445 tion depends on both the image reconstruction quality and precision of the system
446 parameters.
447 We used the phase of the reconstructed results to segment the gold patterns and
448 silicon substrate and calculate the height using the specific method provided in Section
449 S5. Figs.3a and 3b show the surface topography of the regions of number “1” and “2”
450 under the full-pose and no-pose conditions, respectively. These regions correspond to
451 the yellow dashed areas in Fig. 2a. The height map in Fig. 3a exhibits sharp well-
452 defined edges, indicating clear segmentation between the silicon substrate and gold
453 pattern. In contrast, Fig. 3b shows significant glitch artifacts and pattern adhesion,
454 which can be attributed to inaccurate component segmentation caused by poorer
455 image quality. In addition, height histograms are provided to the right of each height
456 map. Both histograms display two distinct peaks corresponding to the heights of the
457 gold pattern and silicon substrate. The distance between the two peaks represent the
458 average height difference between the substrate and pattern, which are 37.53 and 36.86
459 nm for the full-pose and no-pose methods, respectively. Compared to the no-pose
460

Accepted Manuscript

ACCEPTED ARTICLE PREVIEW

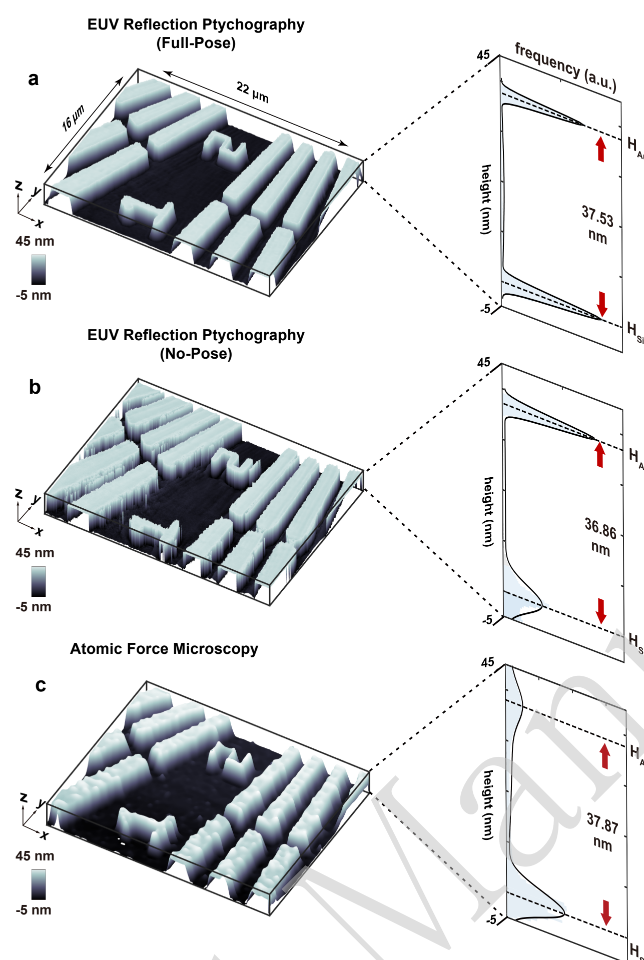

Fig. 3 Surface topography characterization. a, b Height maps in the area marked by a dotted square in Fig. 2a measured by EUV reflection ptychography with and without full-pose calibration. **c** Height maps measured by atomic force microscopy (AFM). Height histograms are provided to the right of each height map.

result, the peaks in the full-pose histogram are sharper, indicating clearer material differentiation. Fig. 3c shows the atomic force microscopy (AFM) measurement results and height distribution of the same sample region, with a peak-to-peak distance of 37.87 nm between the silicon and gold peaks. This height is closer to that measured by the full-pose method. Overall, we demonstrate that full-pose correction is critically important for surface topography characterization.

Accepted Manuscript

ACCEPTED ARTICLE PREVIEW

507
508
509
510
511
512
513
514
515
516
517
518
519
520
521
522
523
524
525
526
527
528
529
530
531
532
533
534
535
536
537
538
539
540
541
542
543
544
545
546
547
548
549
550
551
552

Accepted Manuscript

2.3 Inspection of chip sample

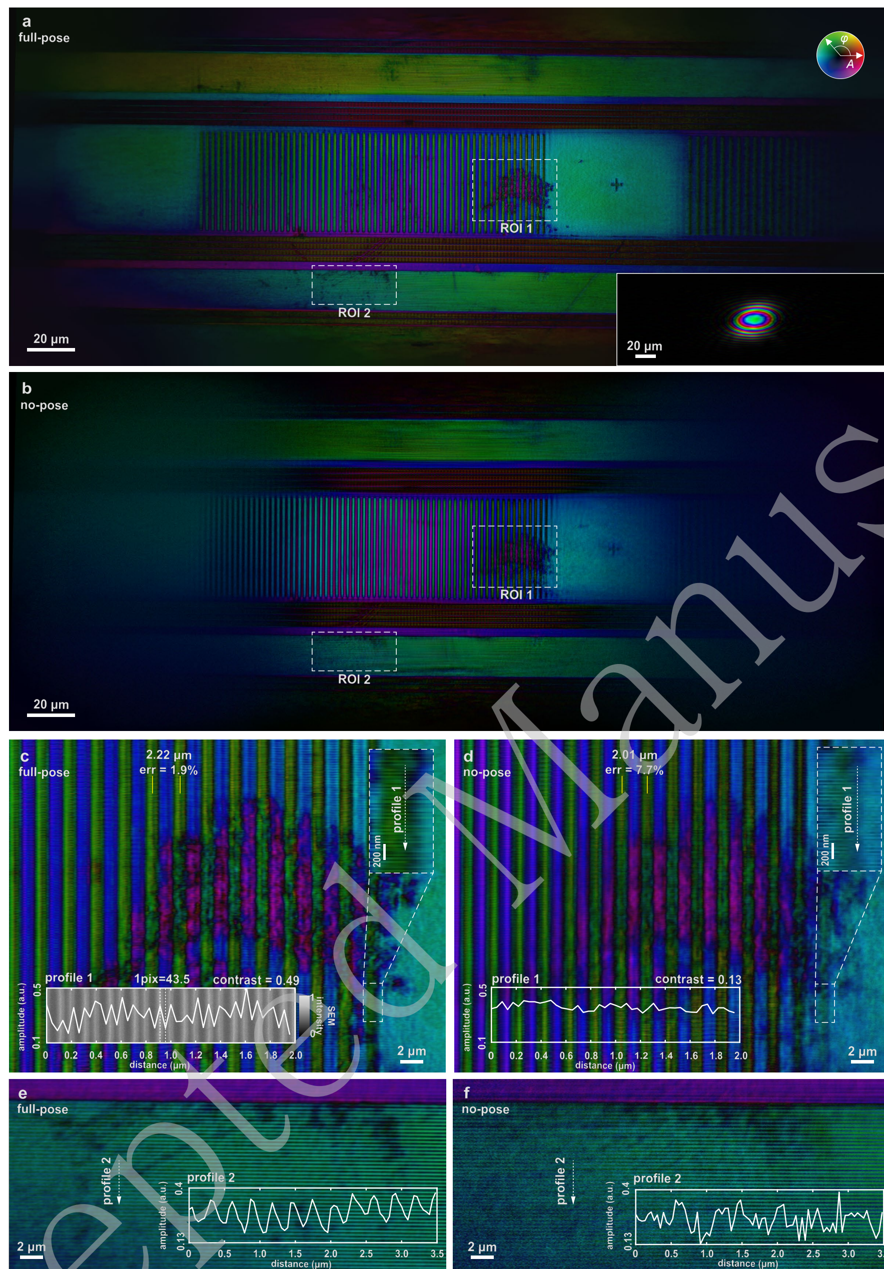

Fig. 4 Inspection on the chip sample. a Full-field pseudocolor result of the chip sample with full-pose calibration and probe image displayed in the bottom-right corner. **b** Full-field pseudocolor result with default parameters (no-pose calibration). **c, d** and **e, f** show magnified views of regions ROI 1 and ROI 2, respectively, reconstructed using full-pose calibration and default parameters (no-pose calibration). The SEM image of the grating area is used as the background of profile 1 in **c** for reference.

553 554 555 556 557 558 559 560 561 562 563 564 565 566 567 568 569 570 571 572 573 574 575 576 577 578 579 580 581 582 583 584 585 586 587 588 589 590 591 592 593 594 595 596 597 598

Accepted Manuscript

ACCEPTED ARTICLE PREVIEW

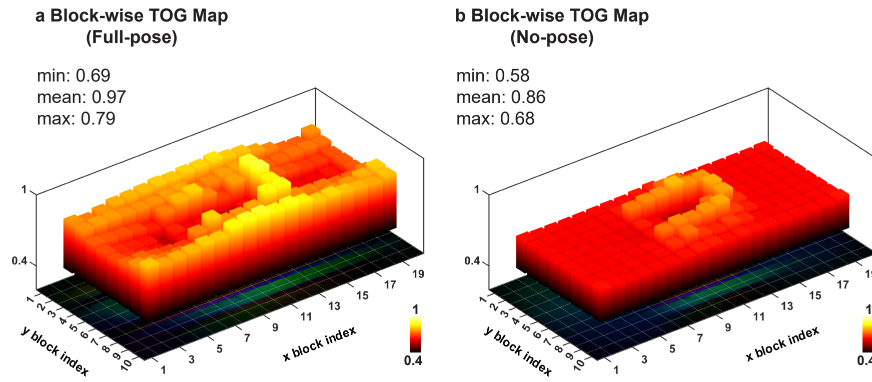

Fig. 5 Block-wise full-field image evaluation of the chip sample. **a** and **b** show the block-wise TOG map corresponding to the reconstructed results with full-pose and no-pose calibration, respectively.

Table 2 Calibrated pose parameter values on the chip sample with different strategies.

	d (mm)	$\boldsymbol{\theta}$ (°)	$\boldsymbol{\gamma}$ (°)
No pose	50.00	[0.00, 70.00, 0.00]	[0.00, 0.00, 0.00]
Full pose	49.87	[-0.35, 71.67, 0.00]	[0.04, 3.45, 0.00]

This system was used to inspect chip samples to demonstrate its practical utility. The sample height variation (within 100 nm) was well within the vertical measurement range of our EUV reflection ptychography system, making it ideally suited for characterization. An SEM image of the chip sample is presented in Fig. S10 in Section S6. The system posture varies because the reinstallation of the clamping mechanism is required for sample replacement, and system hardware such as the camera is reinstalled between the two experiments. Consequently, the system parameters are reconstructed synchronously with the image during the reconstruction process. Parameters with a full-pose calibration and their default values (no pose) are listed in Table 2. Full-field pseudocolor images of the chip sample and illumination probe are shown in Fig. 4 (a) with full-pose calibration, and the non-pose reconstructed image is shown in panel b.

Edge regions exhibited reduced brightness and sharpness compared to that that the center because of the low detection intensity at the FOV periphery. However, the overall structure remained discernible. We magnified the two regions of interest (ROIs) as shown in Figs. 4c–f. Images in Figs. 4c and 4e correspond to results obtained using the full-pose strategy, whereas those in Figs. 4d and 4f correspond to results from the default parameter set (no pose). In ROI1, the chip substrate, grating structures, and contaminants are represented by blue, green, and purple regions, respectively, indicating significant phase variations among these features. In the no-pose result, the boundaries of the purple contaminant regions are noticeably ambiguous, and the green

Accepted Manuscript

ACCEPTED ARTICLE PREVIEW

grating structures in the lower right appear blurred. A comparison of Figs. S10 (b and c) shows that the contamination area in the EUV image with full-pose self-calibration is highly consistent with that in the SEM image. Magnified view in the dashed box highlights the details of the grating structure. Profile 1 shows an amplitude distribution perpendicular to the grating orientation. In the full-pose result, the grating exhibits high contrast (0.49) with the smallest amplitude change corresponding to one pixel (43.5 nm). Fig. S10 b shows an actual grating linewidth of 42.7 nm. The grating area of the SEM image is cropped and used as the background for Profile 1 in Fig. 4 (c) for reference. Although sampling aliasing causes some local contrast loss and slight shifts in peak–valley positions, the EUV ptychography profile accurately matches the grating structure observed in the SEM image. This confirms that the system resolution (half-pitch) reaches a diffraction limit of 43.5 nm. In contrast, the profile at the same location in the no-pose condition shows a significantly lower contrast (0.13).

We measured the distances between adjacent grating regions (marked by solid yellow lines) and obtained values of 2.22 and 2.01 μm using the full-pose and no-pose methods, respectively. Compared with the ground truth of 2.26 μm provided by SEM, the relative errors were 1.9% and 7.7%, respectively. ROI2 was located at the edge of the FOV, where the number of reflected photons was significantly lower than that of ROI1. In Fig. 4f, scratches and grating structures are overwhelmed by noise, whereas in Fig. 4 e, calibrated parameters significantly improve the SNR, which makes both scratches and grating clearly distinguishable. We conducted a full field image quality assessment of the reconstructed image of the chip to demonstrate the improvement achieved through full pose self calibration. Each image was evenly divided into 200 sub regions using a 10×20 grid, as indicated by the dashed lines. The TOG was calculated for every sub region except for those in the outermost border. The resulting TOG values are presented as heatmaps in Figs.6a and b. Visually, the TOG values of the full pose reconstruction are significantly higher across the entire field of view compared to those of the no pose reconstruction. The statistical values of the segmented full-field TOGsuch as the mean are shown in the figures. This blockwise full field evaluation effectively demonstrates the enhancement in image quality caused by full pose self calibration. Our method with full-pose self-calibration enhances the overall SNR of imaging and achieves the best resolution reported to date. Further, the higher-order diffraction signals from the chip sample are stronger than those from the Siemens star sample. The resolution in diffraction imaging depends not only on the NA of the system, but also critically on the SNR of the diffraction signals.

2.4 Consistency of full-pose self-calibration

Unambiguous and unique results are critical for industrial applications, necessitating self-calibration methods that deliver consistent calibration performances across varying conditions. Tests were performed on customized wafer sample data across nine independent runs for the evaluation. Convergence curvatures for different pose parameters are plotted in Figs. 6 (b), and Fig. 6 (a) describes system components that respond to the poses. For each run, initial estimates for d and θ_y were selected randomly from the ranges of 48–50 mm and 70–73 degrees, respectively. In general

Accepted Manuscript

ACCEPTED ARTICLE PREVIEW

691
692
693
694
695
696
697
698
699
700
701
702
703
704
705
706
707
708
709
710

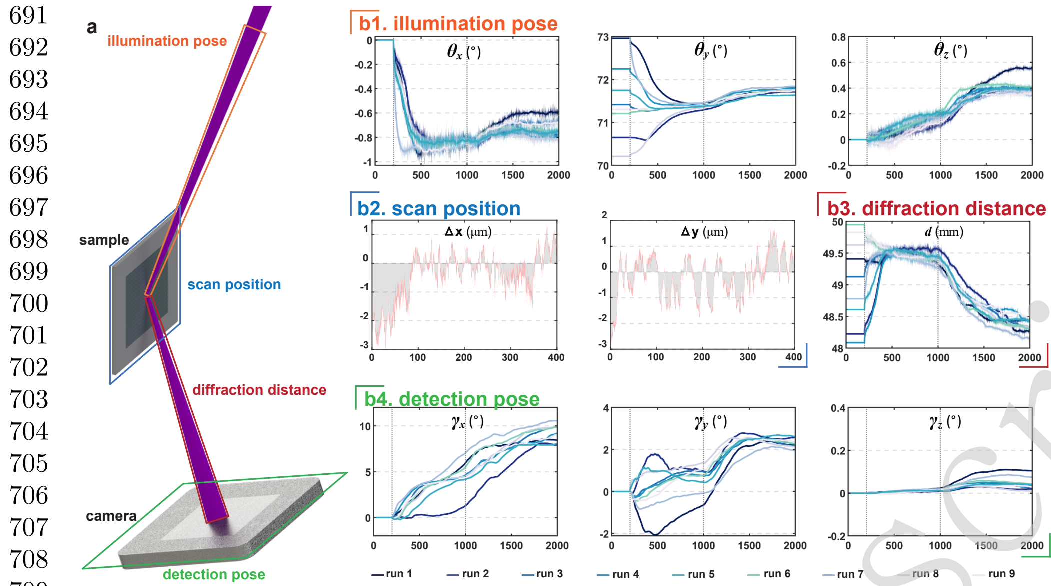

711 **Fig. 6 Consistency test of full-pose self-calibration.a** System components corresponding to
712 different pose parameters. **b1–b4** Convergence of full-pose parameters in nine runs of the algorithm
713 with random initialized d and θ_y. **b1** Convergence curvature of the illumination pose parameters
714 θ_x, θ_y, and θ_z **b2** Corrected position error Δx and Δy of 400 positions. The gray bars indicate
715 the mean value and pink bars represent the corresponding variation. **b3** Convergence curvature of
716 diffraction distance d. **b4** Convergence curvature of detection pose parameters γ_x, γ_y, and γ_z.

717 systems, random initialization is not performed, and the other parameters default to
718 zero.
719 The results confirm that parameter updates exhibit similar convergence trends
720 across runs, yielding final values of $\theta_x = -0.70 \pm 0.12°$, $\theta_y = 71.74 \pm 0.11°$, $\theta_z =$
721 $0.45 \pm 0.10°$, $d = 48.32 \pm 0.17$ mm, $\gamma_x = 9.25 \pm 1.3°$, $\gamma_y = 2.28 \pm 0.34°$, and γ_z
722 consistently below 0.1°. The update behavior of most parameters changed significantly
723 before and after enabling scan position correction at the 1000th epoch. For example,
724 d converges to approximately 49.5 mm before epoch 1000, differing from its final
725 convergence value. This reflects the coupling effect between pose parameters and scan
726 position as discussed in Section S3, which justifies our segmented updating strategy.
727 The corrected position errors (Δx_j, Δy_j) are presented in Fig. 6b, and the gray and
728 pink bars represent the mean value and variation range of the position error across the
729 nine runs. This visualization confirms that the scan position correction is consistent
730 across the nine runs. In conclusion, our full-pose self-calibration method demonstrates
731 strong stability with respect to initial parameter states and consistently converges to
732 uniform calibration results across various scenarios.
733
734
735
736

Accepted Manuscript

ACCEPTED ARTICLE PREVIEW

Table 3 Features of reported reflection ptychography systems on a table-top EUV source

Reported systems	Reflection angle	Wavelength (nm)	method	System self-calibration				Real chip inspection	Half-pitch resolution (nm)
				$\Delta \mathbf{r}_j$	d	θ	γ		
Ref. [27]	moderate (45°)	29.5	ePIE	✗	✗	✗	✗	✗	150
Ref. [28]	moderate (50.5°)	30	ePIE	✗	✗	✗	✗	✗	40
Ref. [29]	high (70°)	29.3	ePIE& rPIE	✗	✗	✗	✗	✗	77.5
Ref. [30]	high (65° - 69°)	29.3	mulptyRAAR	✗	✗	✗	✗	✗	65
Ref. [32]	high (70°)	17.3	AD+SGD	✓	✓	✗	✗	✗	50
Ref. [38]	high (70°)	17.5	AD+Adam	✗	✗	✓	✗	✗	550
this work	high (70°)	17.9	AD+Adam	✓	✓	✓	✓	✓	43.5

Accepted Manuscript

ACCEPTED ARTICLE PREVIEW

783
784
785
786
787
788
789
790
791
792
793
794
795
796
797
798
799
800
801
802
803
804
805
806
807
808
809
810
811
812
813
814
815
816
817
818
819
820
821
822
823
824
825
826
827
828

3 Discussion

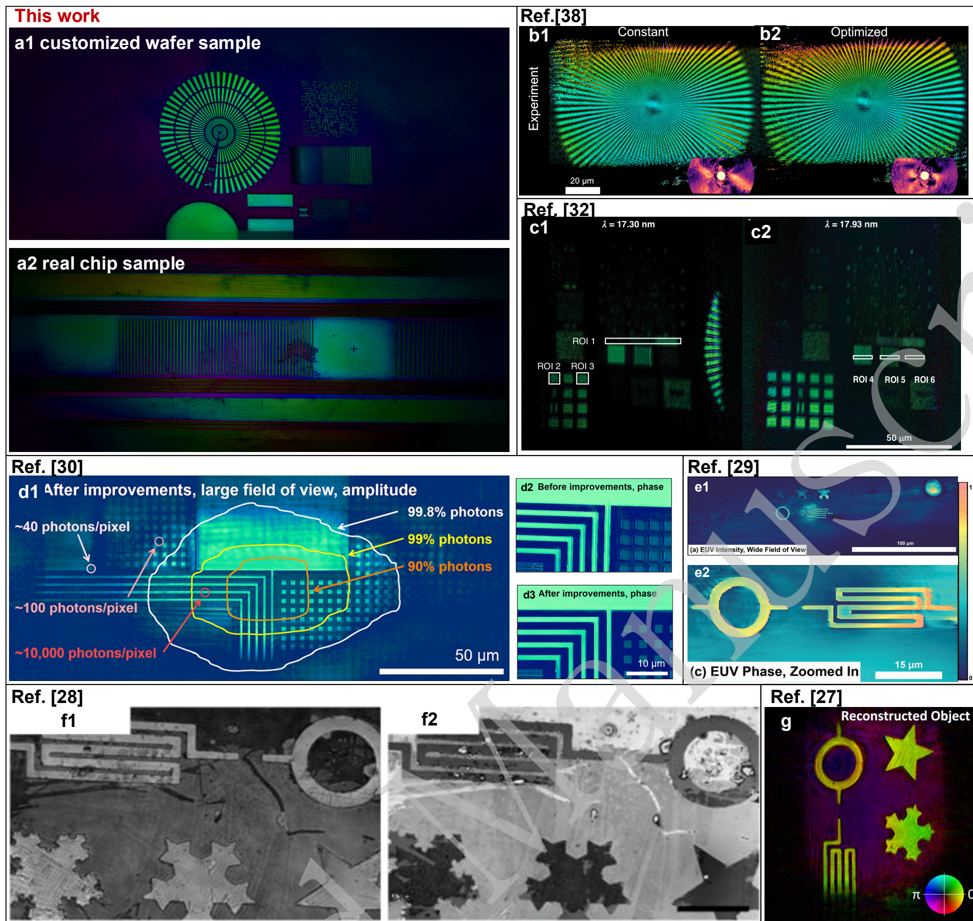

Fig. 7 Representative imaging results of reported reflection ptychography systems based on EUV source. **a1** and **a2** show the full-field results with full-pose calibration in this work. **b1** and **b2** show the pseudocolor imaging results of a Siemens star sample without and with tilt-angle correction adapted from Senhorst *et al.* Opt. Express 32, 44017-44030 (2024) [38].Copyright 2024 Author(s), licensed under a Creative Commons Attribution 4.0 License. **c1** and **c2** are pseudocolor imaging results adapted from Shao *et al.* Light Sci. Appl. 13, 196 (2024) [32]. Copyright 2024 Author(s), licensed under a Creative Commons Attribution 4.0 License. **d1**–**d3** are the amplitude and phase results adapted from Tanksalvala *et al.* Sci. Adv. 7, eabd9667 (2021) [30]. Copyright 2021 Author(s), licensed under a Creative Commons Attribution 4.0 License. **e1** and **e2** show the amplitude and phase results adapted with permission from Poter *et al.* Optica 4, 1552-1557 (2017) [29]. Copyright Optica Publishing Group. **f1** and **f2** show the amplitude and phase results adapted from Zhang *et al.* Ultramicroscopy 158, 98-104 (2015) [28]. Copyright 2015 Author(s), licensed under a Creative Commons Attribution 4.0 License. **g1** represent the pseudocolor result adapted with permission from Seaberg *et al.* Optica 1, 39-44 (2014) [27]. Copyright Optica Publishing Group.

Accepted Manuscript

ACCEPTED ARTICLE PREVIEW

We developed a table-top EUV reflection ptychography system for the simultaneous self-calibration of critical system parameters including the diffraction distance d, three-dimensional illumination angle $\boldsymbol{\theta}$, three-dimensional detection postures $\boldsymbol{\gamma}$, and scan position. This framework demonstrates excellent imaging performance on both customized wafers and real chip samples characterized by robust and consistent self-calibration. The previously reported EUV reflective ptychography systems and their characteristics are summarized in Table 3. For the first time, we integrate the full-pose parameters of a reflection ptychography system into a unified self-calibration framework and demonstrate the universality of our imaging system using both simple (customized wafer) and complex (real chip sample) specimens. To provide an intuitive reference, Fig. 7 juxtaposes representative imaging results from the literature (drawn from the studies compared in Table 3) with those obtained in this study. We acknowledge that a direct quantitative comparison is challenging because of the differences in experimental hardware (e.g., driving laser sources and detectors) and reconstruction software. However, the visual comparison in Fig. 7 clearly demonstrates the significant advancements achieved by the proposed method.

The successful implementation of this approach relies on two elements: comprehensive modeling of the physical system and advanced computational techniques, which include specialized loss functions and robust optimizers. Modeling a full set of system parameters enables synthetic data to progressively approximate real-world physical systems, reducing discrepancy between simulated and actual data. This advancement stems from deeper physical insights and continuous refinements in numerical methods. However, well-designed loss functions and optimizers enable algorithms to maintain strong performance even when synthetic and real-world data cannot be aligned perfectly. The former approach aims to minimize mismatches, whereas the latter enhances robustness against such discrepancies. Our study demonstrates that combining both strategies leads to superior outcomes. This intelligent computing paradigm bridges the gap between physical principles and numerical simulations, paving the way for transformative progress in practical implementations of complex imaging systems. Our research not only advances EUV imaging capabilities but also inspires adaptations across broader imaging modalities and spectral regimes.

Compared to established techniques such as SEM and AFM, a key strength of EUV reflective ptychography is the chemical sensitivity inherent in its phase information. However, unlocking this capability requires angular scanning to acquire the phase–angle spectrum of the sample. Although experiments reported here were performed at a single angle, and thus, they do not fully exploit the material sensitive potential of the technique. We expect that the calibration strategy proposed in this work will still substantially improve the analysis efficiency and accuracy in multiangle scanning scenarios. This stems from the computational efficiency of the automatic differentiation based correction framework and high fidelity imaging enabled by full pose self calibration.

However, practical deployment in online settings is limited by the computational speed of phase retrieval algorithms. Gradient based optimization schemes converge more slowly than the projection based methods. Therefore, future work should focus on integrating full pose learning into accelerated projection based frameworks while

Accepted Manuscript

ACCEPTED ARTICLE PREVIEW

leveraging graphics-processing-unit (GPU) accelerated parallel computing via compute unified device architecture. Such technical advances would enhance computational throughput, paving the way for EUV reflection ptychography to fulfill its potential in industrial metrology.

4 Materials and method

4.1 Derivation of mapping operator T

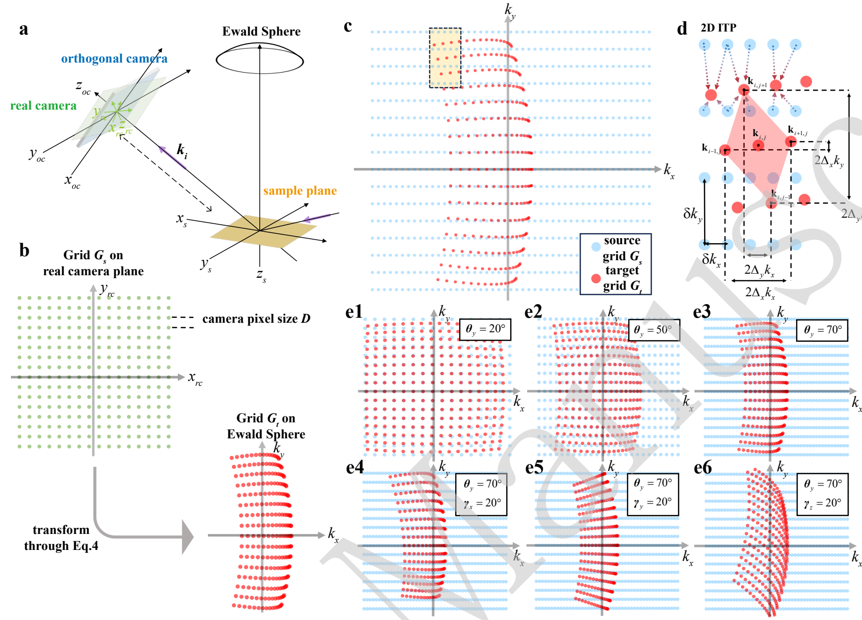

Fig. 8 Sampling grid transformation in the mapping operation **T**. **a** Schematic of tilt detection in reflection ptychography. **b** Grid transformation from real camera plane to Ewald Sphere. The parameters are set to clearly demonstrate the effect of grid warping: wavelength = 17 nm, camera pixel size D = 2200 μm, diffraction distance d = 50 mm, $\theta_y = 70°$, and grid size = 16 × 16. **c** Uniform source and warped target grids on Ewald Sphere. The wavevector range of the source grid is about [-120, 120] rad/μm in both horizontal and vertical directions. **d** Zoom-in region marked by the dotted box in **c** illustrates the procedure of 2D interpolation and parameters used to calculate the Jacobian matrix. The Jacobian value at the (i,j)-th sampling point is determined by the coordinates of its four neighboring sampling points. **e1**–**e6** show grid settings with different pose parameters.

The mapping operator **T** transforms the pattern from an Ewald sphere into a real detection plane via fast interpolation. We establish the transformation relationship of the sampling grid from the real camera coordinate system (x_{rc}, y_{rc}, z_{rc}) to the sample coordinate system (x_s, y_s, z_s), as shown in Fig. 8 a. In a well-aligned setup, the camera should be orthogonal to the light emitted from the sample; however, achieving this in practice is challenging. We represent the sampling point $\mathbf{p}$ in the actual camera coordinate system as $[\mathbf{p}]_{rc} = [x, y, 0]^\top$. Considering possible three-dimensional rotation

Accepted Manuscript

ACCEPTED ARTICLE PREVIEW

of the camera, its representation in the orthogonal camera coordinate system (x_{oc}, y_{oc}, z_{oc}) is $[\mathbf{p}]_{oc} = \mathbf{R}_{\boldsymbol{\gamma}}[\mathbf{p}]_{rc}$, where $\mathbf{R}_{\boldsymbol{\gamma}}$ represents the coordinate rotation operator as

$$\mathbf{R}_{\boldsymbol{\gamma}} = \begin{bmatrix} 1 & 0 & 0 \\ 0 & \cos\gamma_x & \sin\gamma_x \\ 0 & -\sin\gamma_x & \cos\gamma_x \end{bmatrix} \begin{bmatrix} \cos\gamma_y & 0 & \sin\gamma_y \\ 0 & 1 & 0 \\ -\sin\gamma_y & 0 & \cos\gamma_y \end{bmatrix} \begin{bmatrix} \cos\gamma_z & \sin\gamma_z & 0 \\ -\sin\gamma_z & \cos\gamma_z & 0 \\ 0 & 0 & 1 \end{bmatrix} \quad (3)$$

Further, we represent $\mathbf{p}$ using the global sample coordinate system. Given distance d between the origins of coordinate systems (x_{oc}, y_{oc}, z_{oc}) and (x_s, y_s, z_s), and a three-dimensional transformation with angle $\boldsymbol{\theta}$, the representation of the sampling point in the sample coordinate system is $[\mathbf{p}]_s = \mathbf{R}_{\boldsymbol{\theta}}([\mathbf{p}]_{oc} + \mathbf{d})$, where $\mathbf{d} = [0,\ 0,\ d]^\top$. The coordinate relationship for far-field diffraction is established between the internal coordinates of the sample and reciprocal wavevector coordinates. Therefore, we transform the camera point $\mathbf{p}$ into the corresponding wavevector coordinate $\mathbf{k} = k_0[\mathbf{p}]_s/|[\mathbf{p}]_s|$, where $k_0 = 2\pi/\lambda$. The probe illuminates the sample at a grazing angle, and therefore, the tilt phase causes a shift in the diffraction pattern during the Fourier transform. We add the illumination wavevector $\mathbf{k}_i = [\cos\theta_x\sin\theta_y, \sin\theta_x, \cos\theta_x\cos\theta_y]^\top$ in the wavevector coordinate transformation to counteract this shift: $\mathbf{k} = k_0[\mathbf{p}]_s/|[\mathbf{p}]_s| + \mathbf{k}_i$. In summary, the coordinate transformation for a sampling point can be expressed as

$$\mathbf{k} = k_0 \cdot \mathrm{unit}[\mathbf{R}_{\boldsymbol{\theta}}(\mathbf{R}_{\boldsymbol{\gamma}}[\mathbf{p}]_{rc} + \mathbf{d})] + \mathbf{k}_i \quad (4)$$

where unit represents vector normalization $\cdot/|\cdot|$. When the sample thickness is negligible, we require only the first two dimensions (k_x and k_y) of $\mathbf{k}$ to construct a two-dimensional sampling grid. We can derive the warped grid on the Ewald sphere using Eq. 4 by denoting the sampling grid of the real camera G_{rc}; we call this the target grid G_t. An illustration of the grid transformation from G_{rc} to G_t is shown in Fig. 8 b. On the Ewald sphere, we have a uniform source grid G_s, as shown in Fig. 8 (c), which is determined by the sampling conditions on the sample plane. Thus, the complete mapping operator $\mathbf{T}$ can be represented as

$$\mathbf{y} = |\mathrm{det}J| \cdot \mathrm{ITP}(\mathbf{I}, G_s, G_t) \quad (5)$$

where ITP is a two-dimensional (2D) interpolation operator, $\mathbf{y}$ and $\mathbf{I}$ represent the images on tilt detection plane (target) and Ewald sphere (source), and $\mathrm{det}J$ represents the determinant of the Jacobian matrix defined by $\mathrm{det}J = \frac{\partial k_x}{\partial x}\frac{\partial k_y}{\partial y} - \frac{\partial k_x}{\partial y}\frac{\partial k_y}{\partial x}$. To avoid the dimensionality issue and cumbersome differentiation in the above equation, we numerically calculate the determinant using G_s and G_t as

$$\mathrm{det}J = \frac{\Delta_x k_x \Delta_y k_y - \Delta_y k_x \Delta_x k_y}{\delta k_{x_0} \delta k_{y_0}} \quad (6)$$

where Δ_x and Δ_y represent the center difference operations along the x- and y-directions, respectively, and δk_{x_0} and δk_{y_0} represent the sample intervals of the uniform grid G_s. These parameters used to calculate the Jacobian matrix are shown in Fig. 8 d. The multiplication operation with $|\mathrm{det}J|$ ensures the conservation of energy between

Accepted Manuscript

ACCEPTED ARTICLE PREVIEW

967 the source $\mathbf{I}$ and target $\mathbf{y}$. Based on the above derivation, we can easily present the sam-
968 pling grid settings for different pose parameters. Figs. 8 e1–e6 show the distributions
969 of the source and target grids on the Ewald sphere for the different pose parameters.
970

971 ## 4.2 Algorithm implementation
972

973 In our forward model incorporating the coordinate mapping operator, sampling on
974 the virtual detection plane requires an explicit definition. The coordinates of the vir-
975 tual plane are represented in the wave vector k space. We employ an anisotropic grid
976 with a sampling interval and dimensions $\delta\mathbf{k}$, $\mathbf{M}$ to accurately match the distorted
977 diffraction patterns in the reflection geometry: $\delta\mathbf{k} = 2\pi D\,[\cos\theta_{x_0},\ \cos\theta_{y_0}]^\top/(\lambda d)$,
978 $\mathbf{M} = [m, \mathrm{round}(m\cos\theta_{x_0}/2\cos\theta_{y_0})]^\top$ where D, m and $\theta_{x_0} = 0°/\theta_{y_0} = 70°$ repre-
979 sent the camera pixel size, vertical dimension of the raw diffraction patterns, and
980 default illumination angles, respectively. The resulting object-plane sampling interval
981 is $2\pi/(\mathbf{M}\odot\delta\mathbf{k})$, which is defined as the standard sampling $\delta\mathbf{p}_{\mathrm{st}}$. Such sampling results
982 in a numerical aperture ratio of 2:1 between the y- and x-directions on the virtual
983 plane, while the numerical aperture in the y-direction is consistent with the physical
984 numerical aperture of the system in the y direction.

985 Three regularization losses are applied beyond the data fidelity term: (1) Probe
986 support: $\|\mathbf{M}_s \odot \mathbf{P}\|_2^2$ with binary mask $\mathbf{M}_s$, centering the probe and suppressing
987 peripheral artifacts; (2) Total variation: $\|\nabla\mathbf{x}\|_1$ for image edge enhancement and noise
988 suppression; (3) Pattern constraint: $\sum_j \|\mathbf{M}_p \odot \mathbf{I}_j\|_2^2$, where $\mathbf{I}_j$ represents the virtual-
989 plane predicted pattern and $\mathbf{M}_p$ represents a binary mask constraining the energy in
990 unmeasured regions.

991 Our algorithm is implemented using the open-source Python package PyTorch
992 and executed on a server with Nvidia A100 GPU. In the experiment, high-resolution
993 reconstruction follows a three-stage framework with low resolution (LR), medium res-
994 olution (ML), and high resolution (HR) stages. In the LR stage, the images and system
995 parameters are reconstructed using 512 × 512 data size with 2000 epochs. All pose
996 parameters (d, $\boldsymbol{\theta}$ and $\boldsymbol{\gamma}$) are updated at the 200th epoch, whereas the scan positions
997 remain fixed until the 1000th epoch. In the ML and RL stages, the variables are fur-
998 ther refined to data sizes of 1024 × 1024 and 1900 × 1900, each with 50 epochs.
999 Camera edge pixels are discarded in the HR stage because of elevated noise levels. We
1000 employ the Adam optimizer [47] with 10 batches per iteration throughout, resetting
1001 the first-order and second-order momenta whenever new variables are activated. The
1002 learning rates for the variables and regularization weighting coefficients are listed in
1003 Tables 2 and 3. The pose parameters do not significantly change during the ML and
1004 HR stages, indicating that they were successfully corrected during the LR stage.
1005

1006 **Supplementary information.** This article has accompanying supplementary files.

1007 **Acknowledgements.** The authors thank the technical support from Hongbo Xie,
1008 Zefan Huang, Guanbo Wang, Chen Li, Xingwang Xie, Huaqiu Liu, Xiaohui Zhang,
1009 Haoyu Wu, Peixiang Xiong, Tianlei Jia and Tianhao Zhang.
1010

1011 **Author contributions.** Y.C., H.X., Q.W., and Y.L. contributed equally to this
1012 study. Y.C. conceived the idea. Y.C., Q.W., L.H., and S.L. performed the reflection

Accepted Manuscript

ACCEPTED ARTICLE PREVIEW

Table 4 Learning rate settings.

Variable	Learning rate
$\mathbf{x}$	1×10^{-2}
$\mathbf{P}$	1×10^{-2}
d	1×10^{2}
$\boldsymbol{\theta}$	1×10^{-3}
$\boldsymbol{\gamma}$	5×10^{-4}
$\Delta\mathbf{r}_j$	5×10^{-3}

Table 5 Regularization coefficient settings.

Regularization	Weighting coefficient
Probe support	1×10^{-2} (LR) 1×10^{-3}(MR) 0(HR)
Total variation	5×10^{-2} (LR) 5×10^{-3} (MR) 1×10^{-4} (HR)
Pattern constraint	5×10^{-2} (LR) 1×10^{-3} (MR) 0 (HR)

ptychography experiments and processed the data. H.X., Z.X., and J.L.[1,3] prepared the EUV beam at 17.9 nm. Y. L., B. L., G. C., J. L. [9], Y. W., and D. W. supported and developed the EUV source system. Y.C., F.W., and Y.S. prepared, revised, and finalized the manuscript. Z.F., X.Z., C.K. and Y.S. conceived the project. Y.S. supervised the study.

Data availability. Data and codes supporting this study are available from the corresponding author upon request.

Conflict of interest. The authors declare no conflicts of interest.

Funding. National Key Research and Development Program of China (Grant No. 2021YFB3602604), National Natural Science Foundation of China (62131011), and Fundamental Research Funds for Central Universities (E3ET6201X2).

References

[1] Orji, N. G. et al. Metrology for the next generation of semiconductor devices. *Nature Electronics* **1**, 532-547 (2018).

Accepted Manuscript

[2] Kline, R. J. et al. X-ray scattering critical dimensional metrology using a compact x-ray source for next generation semiconductor devices. *Journal of Micro/Nanolithography, MEMS, and MOEMS* **16**, 014001 (2017).

[3] Eschen, W. et al. Coherent nanoscale imaging and chemical mapping with compact extreme ultraviolet and soft x-ray sources: review and perspective. *APL Photonics* **10**, 050901 (2025).

[4] Hädrich, S. et al. High photon flux table-top coherent extreme-ultraviolet source. *Nature Photonics* **8**, 779-783 (2014).

[5] Johnson, A. S. et al. Apparatus for soft x-ray table-top high harmonic generation. *Review of Scientific Instruments* **89**, 083110 (2018).

[6] Ghimire, S. & Reis, D. A. High-harmonic generation from solids. *Nature Physics* **15**, 10-16 (2019).

[7] Louis, E. et al. Nanometer interface and materials control for multilayer EUV-optical applications. *Progress in Surface Science* **86**, 255-294 (2011).

[8] Fu, N. et al. EUV lithography: state-of-the-art review. *Journal of Microelectronic Manufacturing* **2**, 19020202 (2019).

[9] Zahlten, C. et al. High-NA EUV lithography: pushing the limits. *Proceedings of SPIE* 11177, 35th European Mask and Lithography Conference (EMLC 2019). Dresden, Germany: SPIE, 2019, 43-51.

[10] Miao, J. W., Sandberg, R. L. & Song, C. Y. Coherent X-ray diffraction imaging. *IEEE Journal of Selected Topics in Quantum Electronics* **18**, 399-410 (2012).

[11] Gardner, D. F. et al. Subwavelength coherent imaging of periodic samples using a 13.5 nm tabletop high-harmonic light source. *Nature Photonics* **11**, 259-263 (2017).

[12] Eschen, W. et al. Material-specific high-resolution table-top extreme ultraviolet microscopy. *Light: Science & Applications* **11**, 117 (2022).

[13] Rodenburg, J. & Maiden, A. Ptychography. in Springer Handbook of Microscopy (eds Hawkes, P. W. & Spence, J. C. H.) (Cham: Springer, 2019), 819-904.

[14] Pfeiffer, F. X-ray ptychography. *Nature Photonics* **12**, 9-17 (2018).

[15] Aidukas, T. et al. High-performance 4-nm-resolution X-ray tomography using burst ptychography. *Nature* **632**, 81-88 (2024).

[16] Miao, J. W. Computational microscopy with coherent diffractive imaging and ptychography. *Nature* **637**, 281-295 (2025).

Accepted Manuscript

[17] Liu, L. et al. Pushing the resolution limit of coherent diffractive imaging. *Light: Science & Applications* **14**, 298 (2025).

[18] Wang, B. et al. Robust and reliable actinic ptychographic imaging of highly periodic structures in EUV photomasks. *Proceedings of SPIE* 12293, Photomask Technology 2022. Monterey, CA, United States: SPIE, 2022, 122930D.

[19] Wang, B. et al. High-fidelity ptychographic imaging of highly periodic structures enabled by vortex high harmonic beams. *Optica* **10**, 1245-1252 (2023).

[20] Baksh, P. D. et al. Quantitative and correlative extreme ultraviolet coherent imaging of mouse hippocampal neurons at high resolution. *Science Advances* **6**, eaaz3025 (2020).

[21] Liu, C. et al. Visualizing the ultra-structure of microorganisms using table-top extreme ultraviolet imaging. *PhotoniX* **4**, 6 (2023).

[22] Zhang, B. S. et al. Ptychographic hyperspectral spectromicroscopy with an extreme ultraviolet high harmonic comb. *Optics Express* **24**, 18745-18754 (2016).

[23] Du, M. et al. High-resolution wavefront sensing and aberration analysis of multi-spectral extreme ultraviolet beams. *Optica* **10**, 255-263 (2023).

[24] Harada, T. et al. Imaging of extreme-ultraviolet mask patterns using coherent extreme-ultraviolet scatterometry microscope based on coherent diffraction imaging. *Journal of Vacuum Science & Technology B* **29**, 06F503 (2011).

[25] Harada, T. et al. Phase imaging of extreme-ultraviolet mask using coherent extreme-ultraviolet scatterometry microscope. *Japanese Journal of Applied Physics* **52**, 06GB02 (2013).

[26] Lee, D. G. et al. Effect of wrinkles on extreme ultraviolet pellicle reflectivity and local critical dimension. *Applied Optics* **61**, 5965-5971 (2022).

[27] Seaberg, M. D. et al. Tabletop nanometer extreme ultraviolet imaging in an extended reflection mode using coherent Fresnel ptychography. *Optica* **1**, 39-44 (2014).

[28] Zhang, B. S. et al. High contrast 3D imaging of surfaces near the wavelength limit using tabletop EUV ptychography. *Ultramicroscopy* **158**, 98-104 (2015).

[29] Porter, C. L. et al. General-purpose, wide field-of-view reflection imaging with a tabletop 13 nm light source. *Optica* **4**, 1552-1557 (2017).

[30] Tanksalvala, M. et al. Nondestructive, high-resolution, chemically specific 3D nanostructure characterization using phase-sensitive EUV imaging reflectometry. *Science Advances* **7**, eabd9667 (2021).

Accepted Manuscript

ACCEPTED ARTICLE PREVIEW

[31] Jørgensen, P. et al. Hard x-ray grazing-incidence ptychography: large field-of-view nanostructure imaging with ultra-high surface sensitivity. *Optica* **11**, 197-204 (2024).

[32] Shao, Y. F. et al. Wavelength-multiplexed multi-mode EUV reflection ptychography based on automatic differentiation. *Light: Science & Applications* **13**, 196 (2024).

[33] Burdet, N. et al. Bragg projection ptychography on niobium phase domains. *Physical Review B* **96**, 014109 (2017).

[34] Maiden, A. M. et al. An annealing algorithm to correct positioning errors in ptychography. *Ultramicroscopy* **120**, 64-72 (2012).

[35] Loetgering, L. et al. zPIE: an autofocusing algorithm for ptychography. *Optics Letters* **45**, 2030-2033 (2020).

[36] Ruan, T. H. et al. Adaptive total variation based autofocusing strategy in ptychography. *Optics and Lasers in Engineering* **158**, 107136 (2022).

[37] Ning, S. C. et al. An integrated constrained gradient descent (iCGD) protocol to correct scan-positional errors for electron ptychography with high accuracy and precision. *Ultramicroscopy* **248**, 113716 (2023).

[38] Senhorst, S. et al. Mitigating tilt-induced artifacts in reflection ptychography via optimization of the tilt angles. *Optics Express* **32**, 44017-44030 (2024).

[39] Chen, C. C. et al. Resolution-enhanced reflection ptychography with axial distance calibration. *Optics and Lasers in Engineering* **169**, 107684 (2023).

[40] De Beurs, A. et al. aPIE: an angle calibration algorithm for reflection ptychography. *Optics Letters* **47**, 1949-1952 (2022).

[41] Maiden, A. M. et al. Superresolution imaging via ptychography. *Journal of the Optical Society of America A* **28**, 604-612 (2011).

[42] Zhang, S. H., Berendschot, T. T. J. M. & Zhou, J. H. ELFPIE: an error-laxity Fourier ptychographic iterative engine. *Signal Processing* **210**, 109088 (2023).

[43] Zhang, S. H. et al. FPM-WSI: Fourier ptychographic whole slide imaging via feature-domain backdiffraction. *Optica* **11**, 634-646 (2024).

[44] Meyer, G. P. An alternative probabilistic interpretation of the Huber loss. *Proceedings of the 2021 IEEE/CVF Conference on Computer Vision and Pattern Recognition (CVPR).* Nashville, TN, USA: IEEE, 2021, 5261-5269.

[45] Huang, X. J. et al. Optimization of overlap uniformness for ptychography. *Optics Express* **22**, 12634-12644 (2014).

Accepted Manuscript

ACCEPTED ARTICLE PREVIEW

[46] Zhang, Y. B. et al. Edge sparsity criterion for robust holographic autofocusing. *Optics Letters* **42**, 3824-3827 (2017).

[47] Kingma, D. P. & Ba, J. Adam: a method for stochastic optimization. *Proceedings of the 3rd International Conference on Learning Representations*. San Diego, CA, USA: ICLR, 2015.

1197 1198 1199 1200 1201 1202 1203 1204 1205 1206 1207 1208 1209 1210 1211 1212 1213 1214 1215 1216 1217 1218 1219 1220 1221 1222 1223 1224 1225 1226 1227 1228 1229 1230 1231 1232 1233 1234 1235 1236 1237 1238 1239 1240 1241 1242

Accepted Manuscript